Geological Journal

Late Miocene constrictional strain in the northern Apennines: A case study from the Barabarca metaconglomerate (Elba Island, Italy)

Journal:	*Geological Journal*
Manuscript ID	GJ-19-0281.R1
Wiley - Manuscript type:	Research Article
Date Submitted by the Author:	03-Feb-2020
Complete List of Authors:	Papeschi, Samuele; Università degli Studi di Pisa, Dipartimento di Scienze della Terra
Keywords:	Finite strain analysis, shear zone, aureole, pluton, deformation, northern Apennines, Verrucano

Late Miocene constrictional strain in the northern Apennines: A case study from the Barabarca metaconglomerate (Elba Island, Italy)

Samuele Papeschi[1]

1. Dipartimento di Scienze della Terra, Pisa University, via Santa Maria 53, 56126 Pisa, Italy

Corresponding author: Samuele Papeschi (s.papeschi@gmail.com)

Abstract

Finite strain analyses were performed in deformed metaconglomerate from the Calamita Unit in the Island of Elba. The Calamita Unit is a synkinematic contact aureole that was shaped by Late Miocene contractional deformation coeval with high-temperature metamorphism. The metaconglomerate occurs as a L-tectonite in the footwall of a major thrust, entirely surrounded by S-tectonites developed in schistose rocks. Object lineations, defined by the preferred orientation of clasts, trend subparallel to the stretching lineations in the associated rocks. Quartz microstructures registered ductile deformation of clasts by grain boundary migration to bulging recrystallization, suggesting temperature decrease during deformation. Rf/ϕ analyses were carried out on three metaconglomerate samples using quartzite clasts as markers. The finite strain data show that the metaconglomerates are strongly deformed in the constrictional field with K values between ~3 and ~7. The constrictional deformation registered by the metaconglomerate with respect to the surrounding metapelites, which likely deformed under plane strain, can be interpreted as the result of flow partitioning in rheologically heterogeneous sequences during deformation. These results suggest the presence of significant strain gradients in the Calamita Unit, strictly associated with heterogeneously distributed ductile shear zones.

Keywords

Finite strain analysis, shear zone, aureole, pluton, deformation, northern Apennines, Verrucano

1. Introduction

From grain- to lithospheric-scale, deformation tends to be heterogeneously distributed in rocks (Ramsay, 1980; Ramsay & Huber, 1983; Ramsay & Graham, 1970; Sibson, 1977; Simpson & De Paor, 1993). Strain partitioning is a result of the heterogeneous nature of rocks, which consists of lenses, layers, and grains characterized by different physical, chemical, and mechanical properties (Carreras, Cosgrove, & Druguet, 2013; Kuiper, Lin, & Jiang, 2011; Lister & Williams, 1983). While we know that strain tends to be partitioned in rocks, it is often difficult or nearly impossible to quantify how much strain has been absorbed by different lithologies. This is both because strain markers are relatively rare in nature, and because tectonites are often overlooked in the field. However, the distribution of tectonites in the field reveals invaluable clues about how the components of strain are partitioned between different lithologies (see Sullivan, 2013).

According to Flinn (1965), flattening strain produces tectonites with well-developed foliations (S-tectonites), while constrictional strain results in lineation-dominated (L-) tectonites. Between these end-members, tectonites containing a foliation and a lineation (SL-, S=L, and LS-tectonites) are thought to be developed under conditions of more-or-less plane strain. Different types of tectonites often coexist associated within the same geological setting. In particular, it is common to find L-tectonites, surrounded by S- or SL-tectonites (e.g. Bhattacharhyya, Dwivedi, & Das, 2015; Collins,

Van Krakendonk, & Teyssier, 1998; Fossen, 1993; Holst & Fossen, 1987; Hudleston, Schultz-Ela, & Southwick, 1988; Kassem & Ring, 2004; Krabbendam & Dewey, 1998; Sullivan, 2008). The presence of localized L-tectonites has been linked to specific geological settings, such as (1) closures of isoclinal folds, (2) shear zones, (3) and around diapirs and plutons (Yang; Jiang, & Lu, 2019; Sullivan, 2013 and references therein). Some authors have suggested that flow partitioning may produce bodies of L-tectonites in competent bodies surrounded by less-competent lithologies (e.g. Sullivan, 2008; Chen, 2014). This has been confirmed, based on multiscale micromechanical approach, by Yang et al. (2019), which showed that L-tectonites produced by strain partitioning tend to develop only in lithologies with moderately strong relative viscosity with respect to their host rocks. According to these authors, stronger lithologies tend not to register enough strain, while softer lithologies always deform in the flattening field.

In the present study, we document an example of heterogeneous deformation, marked by the occurrence of L-tectonites in quartz metaconglomerate surrounded by schistose rocks that deformed as S-tectonites. Finite strain analyses were carried out on the deformed metaconglomerate using quartz clasts as strain markers. The described deformation is associated with a major shear zone developed under high- to low-grade metamorphic conditions, in a cooling contact aureole.

2. Geological outline

The northern Apennines are a fold-and-thrust belt that resulted from the Oligocene closure of the Ligurian Tethys Ocean and the subsequent westward subduction of the Adria microplate beneath the Corsica-Sardinia margin (Boccaletti et al., 1971). The eastward retreat of the hinge of subduction caused the propagation of the northern Apennines towards the east, leading to the Miocene to present-day opening of the northern Tyrrhenian Sea as a back-arc basin in the hinterland sector of the belt (Brunet, Monié, Jolivet, & Cadet, 2000; Jolivet et al., 1998). Intrusive and extrusive bodies of dominant crustal signature, ranging in age from 14 Ma to 0.2-0.3 Ma and interpreted as related to crustal extension, mark the onset of anatectic magmatism in the area (Serri, Innocenti, & Manetti, 1993). Back arc extension occurred discontinuously from Miocene to present-day times, interrupted by at least one episode of shortening in the late Miocene (see Bonini et al., 2014 and references therein), which is well-documented on the Island of Elba.

The Island of Elba, located in the middle of the northern Tyrrhenian Sea, exposes a complete cross section through the W-dipping and E-verging northern Apennine nappe stack. An out-of-sequence thrust, known as the Capo Norsi – Monte Arco Thrust (CN-MAT in Fig. 1), divides the first order nappe pile into an Upper Complex and a Lower Complex. The Upper Complex comprises ocean- and continent- derived units with anchizone- to lower greenschist-facies metamorphism, intruded by Late Miocene intrusives. The Lower Complex comprises two basement-and-cover metamorphic nappes: the lower amphibolite-facies Ortano Unit and the upper-amphibolite facies Calamita Unit, at the bottom of the nappe stack (Fig. 1).

Amphibolite-facies metamorphism in the Lower Complex was caused by the emplacement of shallow ($P < 0.2$ GPa) Late Miocene intrusives which are hidden below the Calamita peninsula (Porto Azzurro pluton in Fig. 1; Barberi et al., 1967; Musumeci & Vaselli, 2012). Monzogranite apophyses and leucogranite dykes, dated between 6.33±0.07 Ma and 5.9±0.2 Ma (Maineri et al., 2003; Musumeci et al., 2015) represent the only exposures of the Porto Azzurro pluton. Metamorphic temperatures exceeded 650-700 °C in the Calamita Unit, where partial melting was recently reported (Papeschi et al., 2019), and were between 400 and 600 °C in the Ortano Unit (Duranti, Palmeri, Pertusati, & Ricci,

1992; Musumeci & Vaselli, 2012). Contact metamorphic parageneses are constrained between 6.76±0.08 Ma ($^{40}Ar/^{39}Ar$ phlogopite age) and 6.23±0.06 Ma ($^{40}Ar/^{39}Ar$ muscovite age) and are corroborated by a 6.40±0.15 Ma U/Pb zircon age (Musumeci et al., 2011, 2015). Earlier blueschist- to greenschist-facies assemblages, dated at 19.68±0.15 Ma ($^{40}Ar/^{39}Ar$ phengite age; Deino et al., 1992) and 19.8 ± 1.4 Ma ($^{40}Ar/^{39}Ar$ glaucophane age; Bianco et al., 2019), are preserved in the northern part of the Ortano Unit (Bianco et al., 2015).

According to Massa et al. (2017), the Lower Complex experienced early Miocene thrusting, ~~followed by~~ middle Miocene extension, and ~~by~~ a renewed phase of contraction in the Late Miocene. ~~Late Miocene top-to-the-E thrusting~~ was coeval with amphibolite-facies contact metamorphism ~~and,~~ consequently, W-dipping thrust shear zones (FSZ: Felciaio Shear Zone and CSZ: Calanchiole Shear Zone; Musumeci & Vaselli, 2012; Musumeci, Mazzarini, & Cruden, 2015; Papeschi, Musumeci, & Mazzarini, 2017, 2018) and large-scale folds (Ripalte antiform; Mazzarini, Musumeci, & Cruden, 2011) ~~developed in the Lower Complex~~. Thrusting led to inverted metamorphic gradients in the Lower Complex and continued after the thermal pulse was over, with the brittle CN-MAT superimposing non-metamorphic rocks of the Upper Complex directly over cordierite-bearing rocks (Musumeci & Vaselli, 2012). The activity of the syn-metamorphic CSZ and FSZ was bracketed between 6.8 and 6.3 Ma (Musumeci et al., 2015), whereas post-metamorphic brittle thrusting of the CN-MAT lasted until 4.9 Ma (Viola et al., 2018). The aforementioned shear zones were crosscut by the low-angle top-to-the-E Zuccale Fault (ZF in Fig. 1; Collettini, Niemeijer, Viti, & Marone, 2009; Smith, Holdsworth, Collettini, & Pearce, 2011). The ZF, whose significance as a detachment or a thrust is debated, slipped after 4.9 Ma, well after the end of contact metamorphism in the area (Viola et al., 2018).

2.1 Structure and deformation of the Calamita Unit

The Calamita Unit (Fig. 1) consists of an early Carboniferous basement made up of andalusite-cordierite-biotite schist and metapsammite, known as the Calamita Schists fm. (Barberi, Innocenti, & Ricci, 1967; Musumeci, Mazzarini, Tiepolo, & Di Vincenzo, 2011), overlain by the cordierite-bearing Triassic Barabarca quartzite fm. and Mesozoic diopside-tremolite marble (Calanchiole marble fm.; Papeschi et al., 2017). Although originally the Calamita Unit was considered as a coherent basement-and-cover nappe (e.g. Trevisan, 1950; Barberi et al., 1967; Garfagnoli et al., 2005), recent studies have shown that the Mesozoic formations are separated from the Calamita Schists fm. by the Late Miocene CSZ (Musumeci & Vaselli, 2012; Papeschi et al., 2017, 2018; Fig. 1, 2a). In particular, the CSZ is localized in 10-15 meters thick mylonitic marbles, dolomitic marbles and cataclastic rocks at the base of the Calanchiole marble fm., ~~lying in the hanging wall of the shear zone.~~ According to Musumeci & Vaselli (2012), the CSZ shows general top-to-the-E kinematics, a W-dipping (10-40°; Fig. 2b) mylonitic foliation, SW-NE trending lineations (Fig. 2c), and causes a repetition of the Calamita Schists fm. over the Calanchiole marble fm. along the Norsi – Calanchiole section (Fig. 1). The activity of the CSZ lasted between 500-600 °C and ~250 °C during cooling of the contact aureole (Musumeci & Vaselli, 2012) and was constrained between 6.76±0.08 Ma ($^{40}Ar/^{39}Ar$ phlogopite age in mylonitic marble; Musumeci et al., 2015) and 6.14±0.64 Ma (K/Ar on authigenic illite in fault gouge; Viola et al., 2018). The ZF, dated to an age < 4.90 Ma, crosscuts the CSZ, superimposing the non-metamorphic Cretaceous Flysch Unit of the Upper Complex directly over the Calamita Unit (Fig. 2a; Musumeci et al., 2015; Viola et al., 2018).

The relationships between the CSZ and the formations belonging to the Calamita Unit are well-visible along the coast from Punta di Zuccale to Peducelli beach (Fig. 2). In the Calanchiole area (Fig. 3a), the CSZ superimposes mylonitic marble (Fig. 3b) and cataclasite, derived from the Calanchiole marble fm., over schist and fractured quartzite (Fig. 3c) belonging to the Barabarca quartzite fm. Further South, at Peducelli beach (Fig. 3d), analogue mylonitic marble, metadolomite and cataclasite (Fig. 3e; Calanchiole marble fm.) are directly superimposed over fractured schist derived from the Calamita Schists fm. (Fig. 3f). In both cases, the main foliation in the footwall and hanging wall rocks is roughly N-S striking and W-dipping and the stretching lineation trends E-W to NE-SW (see Fig. 3a, d and general stereonets in Fig. 2b, c). The relationships between the Calamita Schists fm. and the Barabarca quartzite fm. are not exposed. Based on the different metamorphic grade of these formations, the Barabarca quartzite fm. was interpreted as a 10-50 meters thick tectonic slice below the CSZ, sandwiched between the Calanchiole marble fm. and the Calamita Schists fm. (Papeschi et al., 2017).

2.2 Deformed metaconglomerate from the Barabarca quartzite

The Barabarca quartzite fm. is made up of white to pink quartzite and violet cordierite-bearing schist with lenses of quartz metaconglomerate (Fig. 4a), referred to as anagenite (*Anageniti grossolane* of Rau & Tongiorgi, 1974). Barberi et al. (1967) correlated these rocks with the Carnian Verrucano of mainland Tuscany, marking the onset of the alpine sedimentary cycle ~~after the variscan orogeny~~ (Rau & Tongiorgi, 1974). The quartz-metaconglomerate of the Verrucano deposited in a fluvial system, fed mostly by a cratonic source, and its clasts, showing sub-angular to well-rounded shape, indicate prolonged transport (see Cassinis, Perotti, & Santi, 2018 and references therein). On Elba, outcrops of metaconglomerates belonging to the Barabarca quartzite fm. are exposed along the coast in the Barabarca and Stecchi localities (Fig. 2a, 4a), in the footwall of the ~~Calanchiole Shear Zone~~ (~~CSZ in~~ Fig. 1, 2a). Inland, the metaconglomerates, and the Barabarca quartzite fm. in general, are poorly exposed, due to the presence of a thick cover of Pleistocene aeolian sandstones (e.g. Fig. 4a).

The metaconglomerate lenses contain polycrystalline quartz- and, locally, tourmaline-clasts (*tourmalinoite Auctt.*), ranging in size between some millimeters to several centimeters (Fig. 4b, c), embedded in a quartz-rich matrix, with minor white mica, tourmaline, biotite, cordierite, ilmenite, and hematite. The foliation in the metaconglomerate is marked by sub-millimetric phyllosilicate-rich layers and pressure solution surfaces wrapping the deformed clasts (Fig. 4b). Based on the elongate shape of the clasts and the intensity of the foliation, the metaconglomerate can be classified as a LS- or, less frequently, a L-tectonite, according to the tectonite classification proposed by Ramsay (1967). The L-fabric is defined by the strong preferred orientation of deformed clasts (Fig. 4c), trend~~ing~~ E-W to NE-SW, ~~that~~ are parallel to the mineral lineations in the associated metapelite (Fig. 2c). The latters are characterized by thin alternations of subparallel quartz- and phyllosilicate-rich layers (Fig. 4d), defining the foliation, and contain abundant cordierite and andalusite spots (Fig. 4e). The lineation in the metapelite is marked by elongated quartz-fibers, and, in second order, by elongated aggregates of cordierite and andalusite (Fig. 4e). However, such aggregates are sometimes also randomly oriented, suggesting a heterogeneous partitioning of strain. The metapelites can be classified, hence, as S-tectonites to SL-tectonites, according to Ramsay (1967).

In the investigated area, three samples of quartz-metaconglomerate were collected for finite-strain analysis in all the available coastal outcrops (sampling locations are shown in Fig. 2a). Two thin sections, representative of the metaconglomerate and the associated metapelite, were prepared for

microstructural analysis. The samples are registered on the System for Earth Sample Registration (SESAR) with additional details are available at http://www.geosamples.org/.

3. Microstructural analysis

The metaconglomerate (sample IESP3SP164) shows polycrystalline quartz clasts with very coarse grain size (mm- to cm- sized) surrounded by a medium- to coarse-grained quartz-rich matrix (Fig. 5a). The larger clasts contain single quartz grains measuring up to several millimeters and are commonly boudinated along fractures perpendicular to the foliation (Fig. 5a). Intracrystalline deformation, characterized by structures such as deformation lamellae (Fig. 5a), are frequent in the inner part of the clasts, whereas extensive dynamic recrystallization to medium- to fine-grained (< 150 μm) quartz aggregates appears localized on the edges of deformed clasts and in the surrounding matrix (Fig. 5b). Small clasts (< 1 mm in thickness) are strongly recrystallized, stretched and show grains with irregular, amoeboid to lobate shape, variable grain size (50 to 500 μm) and serrated grain boundaries (Fig. 5c). The deformed clasts are surrounded by micrometric to 0.1-0.2 mm-thick phyllosilicate- and tourmaline-rich layers, containing also tiny quartz grains and defining the foliation (Fig. 5d). Ellipsoidal-shaped sericite aggregates are interpreted as pseudomorphs over former cordierite and/or andalusite grains (Fig. 5d).

The metapelite (sample IESP3SP163), associated to the metaconglomerate, displays a continuous schistosity defined by the preferred orientation of medium- to fine-grained white mica, quartz, albite, biotite and oxides (in modal order; Fig. 5e). Quartz forms thin lenses and recrystallized aggregates with serrated grain boundaries surrounded by lepidoblastic, mica-rich bands, forming anastomosing patterns (Fig. 5e). Coarse-grained (100 – 400 μm) synkinematic porphyroblasts of andalusite and cordierite, with rotated internal foliations defined by inclusions of quartz and oxides, overgrow the main metamorphic foliation (Fig. 5f). Biotite is present as fine-grained stacks, enveloped by the foliation, or, more commonly, as inclusions in cordierite. Chlorite and sericite occur as alteration phases, over cordierite, andalusite, and biotite.

4. Strain analysis

Finite strain analysis was conducted on three samples of quartz metaconglomerate (samples IESP3SP161, IESP3SP162 and IESP3SP164; shown in Fig. 2a), representative of all the exposed outcrops (see Fig. 2a and Fig. 4a), using the Rf/ϕ method and the deformed clasts as strain markers. The Rf/ϕ method relies on several techniques developed to estimate finite strain starting from a dataset of deformed markers, whose shape can be approximated to that of an ellipse (Dunnet, 1969; Lisle, 1977, 1979, 1985; Ramsay, 1967; Shimamoto & Ikeda, 1976), hence suitable for deformed conglomerates.

Samples were prepared cutting two orthogonal slabs parallel to the XZ (perpendicular to foliation, parallel to lineation) and YZ (perpendicular to foliation and lineation) principal planes of the finite strain ellipsoid. The polished slabs were analyzed using the best-fit ellipse tool of the EllipseFit software (Vollmer, 2015) that makes it possible to estimate the aspect ratio (Rf) and the angle with the foliation (ϕ) of each deformed clast. The original orientation (θ) and aspect ratio (Ri) that each deformed object had in the undeformed state are linked to the Rf and ϕ parameters and depend on the axial ratio of the finite strain ellipsoid (Rs). Dunnet (1969) defined a method to plot hyperbolic Ri- and θ-curves for a population of deformed objects in the Rf/ϕ space, which is, however, based on the assumption of initial random distribution. Following Lisle (1985), the Rf values and the number of

objects in a population (n) can be used to derive the harmonic mean H and to perform the symmetry (I_{SYM}) and χ^2 test. H allows to obtain an approximate estimation of Rs, I_{SYM} estimates the statistical quality of a sample. If I_{SYM} is high (above the critical values listed in Lisle, 1985), then the data set is symmetrical and the assumption of initial random distribution is correct (see in detail Lisle, 1977, 1985). Finally, the χ^2 test allows to obtain a precise estimation of Rs, by calculating the family of θ-curves providing the best fit for the data set. The calculation of H, Rs and χ^2 for a given set of Rf/ϕ values was done using the Excel spreadsheet compiled by Chew (2003). The dataset containing the polished slab scans and the finite strain data is available for download at Mendeley Data (http://dx.doi.org/10.17632/ymbcxhpgyr.1).

4.1 Results

The estimated values of H, I_{SYM}, χ^2 and Rs are summarized in Tab. 1, whereas Fig. 6 shows the resulting Rf/ϕ diagrams with Ri- and θ-curves and the vector mean (red lines). The investigated samples are characterized very high values of I_{SYM} (always above 0.89), indicating that the assumption of initial random distribution is correct. This is consistent with the sedimentological data reported from the Verrucano in the northern Apennines, which is characterized by clasts with very weak preferred orientation (e.g. Azzaro et al., 1976; Martini, Rau, & Tongiorgi, 1986; Rau & Tongiorgi, 1974). The samples display high Rf ratio associated with $\phi < 30°$ on XZ sections and low Rf ratio with a complete ϕ spread on YZ sections (Fig. 6). Estimated Rs value range between 2.50 and 2.92 on XZ sections and between 1.17 and 1.38 on YZ sections (Tab. 1). The K value of Flinn (1965) was derived from the Rs value calculated on XZ and YZ sections, based on the χ^2 test, following the relation:

$$K = \frac{Rs_{XY} - 1}{Rs_{YZ} - 1}$$

Where $Rs_{XY}=Rs_{XZ}/Rs_{YZ}$. The calculated K values are 3.29 (IESP3SP161), 6.68 (IESP3SP162) and 2.94 (IESP3SP164), which plot in the constrictional field of Flinn's diagram (Fig. 7). In Fig. 7, the Rs_{XY} and Rs_{YZ} values estimated with the χ^2 test are shown as triangles. For comparison, the squares represent the Rs_{XY} and Rs_{YZ} values based on the harmonic mean H. The samples plot very close in the diagram, suggesting homogeneous strain within the investigated lens of metaconglomerate in the Barabarca quartzite fm.

5. Discussion

5.1 Strain geometry and conditions of strain

The calculated K values indicate constrictional deformation (Fig. 7), consistently with the field evidence of L- and LS-fabric developed in the metaconglomerate (Fig. 4b, c). The object lineations defined by clasts in the metaconglomerate are subparallel to stretching lineations and mineral lineations defined by the high-temperature assemblage, found in the Barabarca quartzite fm., the Calanchiole marble fm., and the Calamita Schists fm. (Fig. 2b, c). This general trend of stretching lineations is consistent with the E-W trend of lineations in the Late Miocene CSZ (Musumeci & Vaselli, 2012) and in the Late Miocene shear zones that characterize the Calamita Schists fm. (Papeschi et al., 2017). Although geometrically linked to the Late Miocene contractional event that affected the Calamita Unit (see Musumeci et al., 2015 and Viola et al., 2018), the reconstructed total

finite-strain ellipsoid marked by the metaconglomerates, might have registered a certain amount of pre-Late Miocene strain, related to regional metamorphism during continental collision in the northern Apennines. It is impossible to quantify the role of the pre-Late Miocene deformation in the Calamita Unit, where thermal metamorphism and deformation nearly erased pre-existing structures (see Papeschi et al., 2017, 2018). However, the Verrucano of mainland Tuscany, where regional metamorphic temperatures were mostly in the range of 350-500 °C (e.g. Franceschelli et al., 1986; Lo Po & Braga, 2014; Molli, Giorgetti, & Meccheri, 2000), is characterized by weakly deformed clasts retaining in large part their original shape and sedimentary features (e.g. Rau & Tongiorgi, 1974; Martini et al., 1986; Cassinis et al., 2018). It is, hence, likely that the metaconglomerate from the Barabarca quartzite fm. was weakly deformed before the contact metamorphic event, and that, hence, its fabric is mostly the result of the Late Miocene shearing related to the CSZ.

Thermal metamorphism might have induced a strong softening of quartz in the cordierite-bearing Barabarca quartzite fm., which allowed deformation to be accommodated within quartz-metaconglomerate. Indeed, deformation temperatures in the range of 400 - 600 °C were suggested for this part of the aureole (Musumeci & Vaselli, 2012, based on the assemblages described by Pattison & Tracy, 1991). The structures preserved in quartz are indicative of dynamic recrystallization with no evidence of annealing or static growth (Fig. 5a, b, c, d). Although quartz microstructures in the cores of the clasts may be inherited from the protolith, extensive recrystallization is evident along the rims (Fig. 5a, b), in strongly stretched quartz, and in the matrix (Fig. 5c, d), domains marking the stretching lineation of these rocks. Such structures are indicative of grain boundary migration recrystallization (amoeboid grain boundaries) overprinted by subgrain rotation and bulging (i.e. equant, serrated grains), based on a comparison with the structures observed by Stipp, Stünitz, Heilbronner, & Schmid (2002). High-temperature microstructures overprinted by low-temperature microstructures in quartz suggest progressive temperature decrease (see also Papeschi et al., 2017), assuming that no significant change in strain rate and presence of water during deformation.

5.2 Origin of L-tectonites surrounded by S-tectonites in the Barabarca quartzite

The general trend of stretching lineations (Fig. 2b, c) and the analysis of deformation mechanisms at the microscale (see above) link the investigated L- and LS-tectonites (Fig. 4b, c) to the activity of the CSZ. Any effect related to pluton ballooning (e.g. Sylvester, Ortel, Nelson, & Christie, 1978; Ramsay, 1989) can be excluded, since object lineations are parallel to shear zone lineations. Furthermore, as documented by Papeschi et al. (2017), the effect of pluton ballooning on the general geometry of structures within the aureole is negligible.

There are several ways in which L-tectonites could have formed on a major shear zone. In first order, the activity of the CSZ might have caused buckling of the competent metaconglomerate, producing isoclinal folds. In this case, object lineations would have been parallel to the fold axes, hence roughly perpendicular to the stretching lineations related to the CSZ (Fig. 8a; see examples in Fossen, 1993: Holst & Fossen, 1987; Liu, Lin, & Song, 2017). This situation is in contrast with the observed parallelism between object and stretching lineations (e.g. Fig. 2c). Moreover, the presence of folds, would produce a gradient between hinge zones, where L-tectonites would form, and limbs, that would experience deformation under conditions of plane strain, which are not present in the study area.

The localization of L- and LS-tectonites within homogeneous and competent lithologies surrounded by heterogeneous and incompetent lithologies that developed S- and SL-tectonites is similar to the example described by Sullivan (2008). According to this author, constriction in the Raft River shear

zone (Utah) was absorbed by more competent metaconglomerates, while simple shear concentrated within rheologically weak phyllonites. A similar example was flagged by Yang et al. (2019), which showed L-fabrics developed in rheologically strong granites surrounded by schistose rocks in the Dakendaban complex (China). Also, Yang et al. (2019), suggested a possible origin by strain partitioning, with constriction localized in competent layers and flattening localized in incompetent rocks. This could be the case also for the described metaconglomerate from the footwall of the CSZ. In particular, the parallelism of object lineations in L-tectonites with stretching lineations in associated lithologies and in the overlying CSZ (Fig. 8b) points to a macroscale flow close to plane-strain general shearing, in agreement with Yang et al. (2019).

Strikingly different tectonites in associated competent and competent lithologies can hence be explained as a result of strain partitioning (Fig. 8b), as it is commonly documented also for folding, boudinage, and foliation development (e.g. Holst & Fossen, 1987; Smith, 1975; Treagus, 1988). Stretching lineations in incompetent metapelites tend to form, at the outcrop- to micro-scale (see also Fig. 4e), in more competent layers/domains that may stretch within incompetent, platy phyllosilicates. At larger scale, a strongly competent body surrounded by incompetent rocks, would tend to register the constrictional component of strain in a similar fashion, developing a strong lineated fabric within incompetent rocks that mostly register flattening.

6. Conclusions

This study provides new microstructural and finite strain data regarding a deformed metaconglomerate from the Calamita Unit (Island of Elba, Italy), showing evidence of Late Miocene deformation related to coeval contractional tectonics and high-temperature metamorphism related to the emplacement of intrusives. Quartz microstructures and metamorphic paragenesis are consistent with deformation under medium-grade conditions. The metaconglomerate was deformed in the constrictional field with K values between 2.94 and 6.68, while the surrounding metapelite developed S- to SL- tectonite fabric. The contrasting L-tectonite fabric of the metaconglomerate and S-tectonite fabric of the metapelite suggest flow partitioning during deformation, between competent and incompetent lithologies.

Acknowledgements

I wish to thank Giovanni Musumeci and Francesco Mazzarini for field support during sampling and for the constructive reviews on an earlier version of this manuscript. I also thank Giulio Viola and an anonymous reviewer for their constructive reviews, and Chiara Frassi for editorial handling. This work received funding from PRA_2016 (Resp. Sergio Rocchi) funds of the University of Pisa.

References

Azzaro, E., Cocozza, T., Di Sabatino, B., Gasperi, G., Gelmini, R., & Lazzarotto, A. (1976). Geology and petrography of the Verrucano and Paleozoic formations of Southern Tuscany and Northern Latium (Italy). In: Falke, H. (Ed.). *The Continental Permain in Central, West, and South Europe* (pp. 181-195). Proceedings of the NATO Advanced Study Institute held at the Johannes Gutenberg University, Mainz, F.R.G., 23. September – 4 October, 1975. Springer, Dordrecht.

Barberi, F., Innocenti, F., Ricci, C.A., 1967. Il complesso scistoso di Capo Calamita (Isola d'Elba). *Atti della Società Toscana di Scienze Naturali residente a Pisa, Memorie, Serie A 72 (2)*, 579–617.

Bhattacharyya, K., Dwivedi, H. V., Das, J. P., & Damania, S. (2015). Structural geometry, microstructural and strain analyses of L-tectonites from Paleoproterozoic orthogneiss: Insights into local transport-parallel constrictional strain in the Sikkim Himalayan fold thrust belt. *Journal of Asian Earth Sciences*, *107*, 212-231.

Bianco, C., Brogi, A., Caggianelli, A., Giorgetti, G., Liotta, D., & Meccheri, M. (2015). HP-LT metamorphism in Elba Island: implications for the geodynamic evolution of the inner Northern Apennines (Italy). *Journal of Geodynamics*, *91*, 13-25.

Boccaletti, M., Elter, P., & Guazzone, G. (1971). Plate tectonic models for the development of the Western Alps and Northern Apennines. *Nature Physical Science*, *234*(49), 108-111.

Bonini, M., Sani, F., Stucchi, E. M., Moratti, G., Benvenuti, M., Menanno, G., & Tanini, C. (2014). Late Miocene shortening of the Northern Apennines back-arc. *Journal of Geodynamics*, *74*, 1-31.

Brunet, C., Monié, P., Jolivet, L., & Cadet, J. P. (2000). Migration of compression and extension in the Tyrrhenian Sea, insights from $^{40}Ar/^{39}Ar$ ages on micas along a transect from Corsica to Tuscany. *Tectonophysics*, *321*(1), 127-155.

Carreras, J., Cosgrove, J. W., & Druguet, E. (2013). Strain partitioning in banded and/or anisotropic rocks: Implications for inferring tectonic regimes. *Journal of Structural Geology*, *50*, 7-21.

Cassinis, G., Perotti, C., & Santi, G. (2018). Post-Variscan Verrucano-like deposits in Italy, and the onset of the alpine tectono-sedimentary cycle. *Earth-science reviews*, *185*, 476-497.

Chen, W. (2014). The Development of L-tectonites in High-strain Zone Settings: A Multiscale Modeling Investigation. Master Dissertation. The University of Western Ontario, 1-116.

Chew, D. M. (2003). An Excel spreadsheet for finite strain analysis using the Rf/φ technique. *Computers & geosciences*, *29*(6), 795-799.

Collettini, C., Niemeijer, A., Viti, C., & Marone, C. (2009). Fault zone fabric and fault weakness. *Nature*, *462*(7275), 907.

Collins, W. J., Van Kranendonk, A. M., & Teyssier, C. (1998). Partial convective overturn of Archaean crust in the east Pilbara Craton, Western Australia: driving mechanisms and tectonic implications. *Journal of Structural Geology*, *20*(9-10), 1405-1424.

Dunnet, D. (1969). A technique of finite strain analysis using elliptical particles. *Tectonophysics*, *7*(2), 117-136.

Duranti, S., Palmeri, R., Pertusati, P. C., & Ricci, C. A. (1992). Geological evolution and metamorphic petrology of the basal sequences of eastern Elba (complex II). *Acta Vulcanologica*, *2*, 213-229.

Flinn, D. (1965). On the symmetry principle and the deformation ellipsoid. *Geological magazine*, *102*(1), 36-45.

Fossen, H. (1993). Linear fabrics in the Bergsdalen nappes, southwest Norway: implications for deformation history and fold development. *Norsk Geologisk Tidsskrift, 73,* 95-108.

Franceschelli, M., Leoni, L., Memmi, I., & Puxeddu, M. (1986). Regional distribution of Al-silicates and metamorphic zonation in the low-grade Verrucano metasediments from the northern Apennines, Italy. *Journal of Metamorphic Geology*, *4*(3), 309-321.

Holst, T. B., & Fossen, H. (1987). Strain distribution in a fold in the West Norwegian Caledonides. *Journal of structural geology*, *9*(8), 915-924.

Hudleston, P. J., Schultz-Ela, D., & Southwick, D. L. (1988). Transpression in an Archean greenstone belt, northern Minnesota. *Canadian Journal of Earth Sciences*, *25*(7), 1060-1068.

Jolivet, L., Faccenna, C., Goffé, B., Mattei, M., Rossetti, F., Brunet, C., ... & Parra, T. (1998). Midcrustal shear zones in postorogenic extension: example from the northern Tyrrhenian Sea. *Journal of Geophysical Research: Solid Earth*, *103*(B6), 12123-12160.

Kassem, O., & Ring, U. (2004). Underplating-related finite-strain patterns in the Gran Paradiso massif, Western Alps, Italy: heterogeneous ductile strain superimposed on a nappe stack. *Journal of the Geological Society*, *161*(5), 875-884.

Keller, J. V. A., & Coward, M. P. (1996). The structure and evolution of the Northern Tyrrhenian Sea. *Geological Magazine*, *133*(1), 1-16.

Krabbendam, M., & Dewey, J. F. (1998). Exhumation of UHP rocks by transtension in the Western Gneiss Region, Scandinavian Caledonides. *Geological Society, London, Special Publications*, *135*(1), 159-181.

Kuiper, Y. D., Lin, S., & Jiang, D. (2011). Deformation partitioning in transpressional shear zones with an along-strike stretch component: An example from the Superior Boundary Zone, Manitoba, Canada. *Journal of Structural Geology*, *33*(3), 192-202.

Law, R. D. (1987). Heterogeneous deformation and quartz crystallographic fabric transitions: natural examples from the Moine Thrust zone at the Stack of Glencoul, northern Assynt. *Journal of Structural Geology*, *9*(7), 819-833.

Lin, S., and Jiang, D. (2001). Using along-strike variation in strain and kinematics to define the movement direction of curved transpressional shear zones: An example from northwestern Superior Province, Manitoba. *Geology, 29(9),* 767-770.

Lisle, R. J. (1977). Estimation of the tectonic strain ratio from the mean shape of deformed elliptical markers. *Geologie en Mijnbouw*, *56*(2), 140-144.

Lisle, R. J. (1979). Strain analysis using deformed pebbles: the influence of initial pebble shape. *Tectonophysics*, *60*(3-4), 263-277.

Lisle, R. J. (1985). Geological Strain Analysis: A Manual for the Rf/0 Technique. Pergamon Press.

Lister, G. S., & Williams, P. F. (1983). The partitioning of deformation in flowing rock masses. *Tectonophysics*, *92*(1-3), 1-33.

Liu, H., Lin, S., & Song, C. (2017). Orogen-scale L tectonite domain in the Tongbai orogenic belt, central China: Geological setting and origin. *Journal of Structural Geology*, *94*, 184-194.

Lo Pò, D., & Braga, R. (2014). Influence of ferric iron on phase equilibria in greenschist facies assemblages: the hematite-rich metasedimentary rocks from the Monti Pisani (Northern Apennines). *Journal of Metamorphic Geology*, *32*(4), 371-387.

Martini, I. P., Rau, A., & Tongiorgi, M. (1986). Syntectonic sedimentation in a Middle Triassic rift, northern Apennines, Italy. *Sedimentary Geology*, *47*(3-4), 191-219.

Mazzarini, F., Musumeci, G., & Cruden, A. R. (2011). Vein development during folding in the upper brittle crust: The case of tourmaline-rich veins of eastern Elba Island, northern Tyrrhenian Sea, Italy. *Journal of Structural Geology*, *33*(10), 1509-1522.

Molli, G., Giorgetti, G., & Meccheri, M. (2000). Structural and petrological constraints on the tectono-metamorphic evolution of the Massa Unit (Alpi Apuane, NW Tuscany, Italy). *Geological Journal*, *35*(3-4), 251-264.

Musumeci, G., & Vaselli, L. (2012). Neogene deformation and granite emplacement in the metamorphic units of northern Apennines (Italy): Insights from mylonitic marbles in the Porto Azzurro pluton contact aureole (Elba Island). *Geosphere*, *8*(2), 470-490.

Musumeci, G., Mazzarini, F., Tiepolo, M., & Di Vincenzo, G. (2011). U-Pb and ^{40}Ar-^{39}Ar geochronology of Palaeozoic units in the northern Apennines: determining protolith age and alpine evolution using the Calamita Schist and Ortano Porphyroid. *Geological Journal*, *46*(4), 288-310.

Musumeci, G., Mazzarini, F., & Cruden, A. R. (2015). The Zuccale Fault, Elba Island, Italy: a new perspective from fault architecture. *Tectonics*, *34*(6), 1195-1218.

Papeschi, S., Musumeci, G., & Mazzarini, F. (2017). Heterogeneous brittle-ductile deformation at shallow crustal levels under high thermal conditions: The case of a synkinematic contact aureole in the inner northern Apennines, southeastern Elba Island, Italy. *Tectonophysics*, *717*, 547-564.

Papeschi, S., Musumeci, G., & Mazzarini, F. (2018). Evolution of shear zones through the brittle-ductile transition: The Calamita Schists (Elba Island, Italy). *Journal of Structural Geology*, *113*, 100-114.

Pattison, D. R. M., & Tracy, R. J. (1991). Phase equilibria and thermobarometry of metapelites. In: Derrill, M.K. (Ed.), *Contact Metamorphism*. Reviews in Mineralogy, Mineralogical Society of America Vol. 26.

Ramsay, J. G. (1967). Folding and fracturing of rocks. Mc Graw Hill.

Ramsay, J. G. (1980). Shear zone geometry: a review. *Journal of structural geology*, *2*(1-2), 83-99.

Ramsay, J. G. (1989). Emplacement kinematics of a granite diapir: the Chindamora batholith, Zimbabwe. *Journal of Structural Geology*, *11*(1-2), 191-209.

Ramsay, J. G., & Graham, R. H. (1970). Strain variation in shear belts. *Canadian Journal of Earth Sciences*, *7*(3), 786-813.

Ramsay, J. G., & Huber, M. I. (1983). The techniques of modern structural geology: strain analysis (Vol. 1). Academic press.

Rau, A., & Tongiorgi, M. (1974). Geologia dei Monti Pisani a sud-est della Valle del Guappero. Arti grafiche Pacini Mariotti.

Serri, G., Innocenti, F., & Manetti, P. (1993). Geochemical and petrological evidence of the subduction of delaminated Adriatic continental lithosphere in the genesis of the Neogene-Quaternary magmatism of central Italy. *Tectonophysics*, *223*(1-2), 117-147.

Shimamoto, T., & Ikeda, Y. (1976). A simple algebraic method for strain estimation from deformed ellipsoidal objects. 1. Basic theory. *Tectonophysics*, *36*(4), 315-337.

Sibson, R. H. (1977). Fault rocks and fault mechanisms. *Journal of the Geological Society*, *133*(3), 191-213.

Simpson, C., & De Paor, D. G. (1993). Strain and kinematic analysis in general shear zones. *Journal of Structural Geology*, *15*(1), 1-20.

Smith, R. B. (1975). Unified theory of the onset of folding, boudinage, and mullion structure. *Geological Society of America Bulletin*, *86*(11), 1601-1609.

Smith, S. A. F., Holdsworth, R. E., Collettini, C., & Pearce, M. A. (2011). The microstructural character and mechanical significance of fault rocks associated with a continental low-angle normal fault: the Zuccale Fault, Elba Island, Italy. *Geological Society, London, Special Publications*, *359*(1), 97-113.

Stipp, M., Stünitz, H., Heilbronner, R., & Schmid, S. M. (2002). The eastern Tonale fault zone: a 'natural laboratory' for crystal plastic deformation of quartz over a temperature range from 250 to 700 C. *Journal of Structural Geology*, *24*(12), 1861-1884.

Sullivan, W. A. (2008). Significance of transport-parallel strain variations in part of the Raft River shear zone, Raft River Mountains, Utah, USA. *Journal of Structural Geology*, *30*(2), 138-158.

Sullivan, W. A. (2013). L tectonites. *Journal of structural geology*, *50*, 161-175.

Sylvester, A. G., Ortel, G., Nelson, C. A., & Christie, J. M. (1978). Papoose Flat pluton: A granitic blister in the Inyo Mountains, California. *Geological Society of America Bulletin*, *89*(8), 1205-1219.

Treagus, S. H. (1988). Strain refraction in layered systems. *Journal of Structural Geology*, *10*(5), 517-527.

Viola, G., Torgersen, E., Mazzarini, F., Musumeci, G., van der Lelij, R., Schönenberger, J., & Garofalo, P. S. (2018). New Constraints on the Evolution of the Inner Northern Apennines by K-Ar Dating of Late Miocene-Early Pliocene Compression on the Island of Elba, Italy. *Tectonics*, *37*(9), 3229-3243.

Vitale, S., & Mazzoli, S. (2009). Finite strain analysis of a natural ductile shear zone in limestones: insights into 3-D coaxial vs. non-coaxial deformation partitioning. *Journal of Structural Geology*, *31*(1), 104-113.

Vollmer, F. W. (2015). EllipseFit 2.0.

Xypolias, P., & Kokkalas, S. (2006). Heterogeneous ductile deformation along a mid-crustal extruding shear zone: an example from the External Hellenides (Greece). *Geological Society, London, Special Publications*, *268*(1), 497-516.

Yang, R., Jiang, D., & Lu, L. X. (2019). Constrictional strain and linear fabrics as a result of deformation partitioning: a multiscale modeling investigation and tectonic significance. *Tectonics*, *38*(8), 2829-2849.

Table 1 – Summary of the results of finite strain analysis. n is the population of measured strain markers. See text for further details.

Sample	section	n	H	I_{SYM}	χ^2 min	Rs
SP161	XZ	84	2.7167	0.9524	5.0476	2.65
	YZ	88	1.4324	0.9090	9.0455	1.31
SP162	XZ	74	2.6298	0.9189	7.6216	2.50
	YZ	56	1.3511	0.8929	4.3571	1.17
SP164	XZ	69	3.0102	0.8985	0.7101	2.92
	YZ	67	1.5535	0.9552	2.7015	1.38

Figure captions

Figure 1 – Simplified structural-geological map of the Calamita peninsula (SE Island of Elba), showing the location of the study area. Abbreviations: CN-MAT: Capo Norsi-Monte Arco Thrust; CSZ: Calanchiole Shear Zone; FSZ: Felciaio Shear Zone. Mineral abbreviations are Ab: albite; And: andalusite; Bi: biotite; Cd: cordierite; Di: diopside; Ksp: K-feldspar; Phl: phlogopite; Tr: tremolite; Wo: wollastonite.

Figure 2 – Detail of the study area. **(a)** Sketch geological map of the Barabarca area showing the location of figures and samples. **(b-c)** Stereographic projections (equal area, lower hemisphere) showing **(b)** poles to foliation and **(c)** stretching lineations.

Figure 3 – Relationships between the Calanchiole Shear Zone, the Barabarca quartzite fm., and the Calamita Schists fm., at **(a-b-c)** Calanchiole and **(d-e-f)** Peducelli beaches. **(a-d)** Panoramic views. **(b)** Stretching lineations, defined by aggregates of dolomite and calcite, in mylonitic marble. **(c)** Fractured quartzite and schist belonging to the Barabarca quartzite fm. **(e)** Ultramylonitic marble with boudinated lenses of metadolomite. **(f)** Riedel shears in the Calamita Schists fm., consistent with overall top-to-the-E sense of shear. Stereographic projections are equal area, lower hemisphere. Circles represent poles to the foliation in the Calanchiole marble fm. (light blue), the Barabarca quartzite fm. (pink), and the Calamita Schists fm. (violet). Crosses are stretching lineations in the Calanchiole marble fm. (blue), the Barabarca quartzite fm. (red), and the Calamita Schists fm. (black) See text for a detailed comment. Measurements from the Calanchiole area after Musumeci & Vaselli (2012).

Figure 4 – Details of the investigated outcrops, hosting the metaconglomerate. **(a)** Panoramic view of the Barabarca gulf, showing the relationships between metaconglomerate, quartzite, and schist in the Barabarca quartzite fm. The red dashed line highlights the projected location of the Calanchiole Shear Zone. **(b-c)** Outcrop appearance of the deformed quartz metaconglomerate, showing **(b)** L-tectonite fabric and **(c)** LS-tectonite fabric. **(d-e)** Metapelite associated with the metaconglomerate. Note **(d)** the strong planar fabric, and (e) the presence of stretching lineations defined by quartz fibers and alignments of andalusite (And) - cordierite (Cd) spots.

Figure 5 – Representative microstructures of the Barabarca quartzite fm. The yellow dashed line marks the foliation. **(a-b-c-d)** Quartz metaconglomerate (IESP3SP164): **(a)** large quartz clasts wrapped by a fine-grained foliated quartz matrix showing boudinage structures (violet arrow); **(b)** detail of the edge of a deformed quartz clast showing extensive recrystallization; **(c)** stretched, ribbon-like, quartz clast with amoeboid to lobate boundaries, interlayered with sericite and tourmaline-rich layers; **(d)** sericitized cordierite and white mica-rich layers associated with tourmaline grains. **(e-f)** Metapelite (IESP3SP163): **(e)** detail of the main foliation, defined by the preferred orientation of quartz and phyllosilicates; **(f)** synkinematic andalusite porphyroblast with rotated internal foliation. And: andalusite; Cd: cordierite. Tur: tourmaline; Wm: white mica.

Figure 6 – Detail of the Rf/φ plots used for finite strain analyses on the metaconglomerate samples. Ri contours are shown in blue for Ri = 1.25, 1.5, 1.75, 2, 2.5, 3, 4 and 6. The θ-curves are shown in violet. Red lines represent the vector mean.

Figure 7 – Results of the finite strain analyses plotted on the Flinn diagram. For each sample, Rs_{XY} and Rs_{YZ} were calculated based on the harmonic mean method (squares) and the χ^2 test (triangles).

Figure 8 – Block diagrams illustrating the different relationships between object and stretching lineations in the case of **(a)** constriction by folding in a shear zone and **(b)** constriction related to strain partitioning in a shear zone. Fig. **8a** modified after Sullivan (2013).

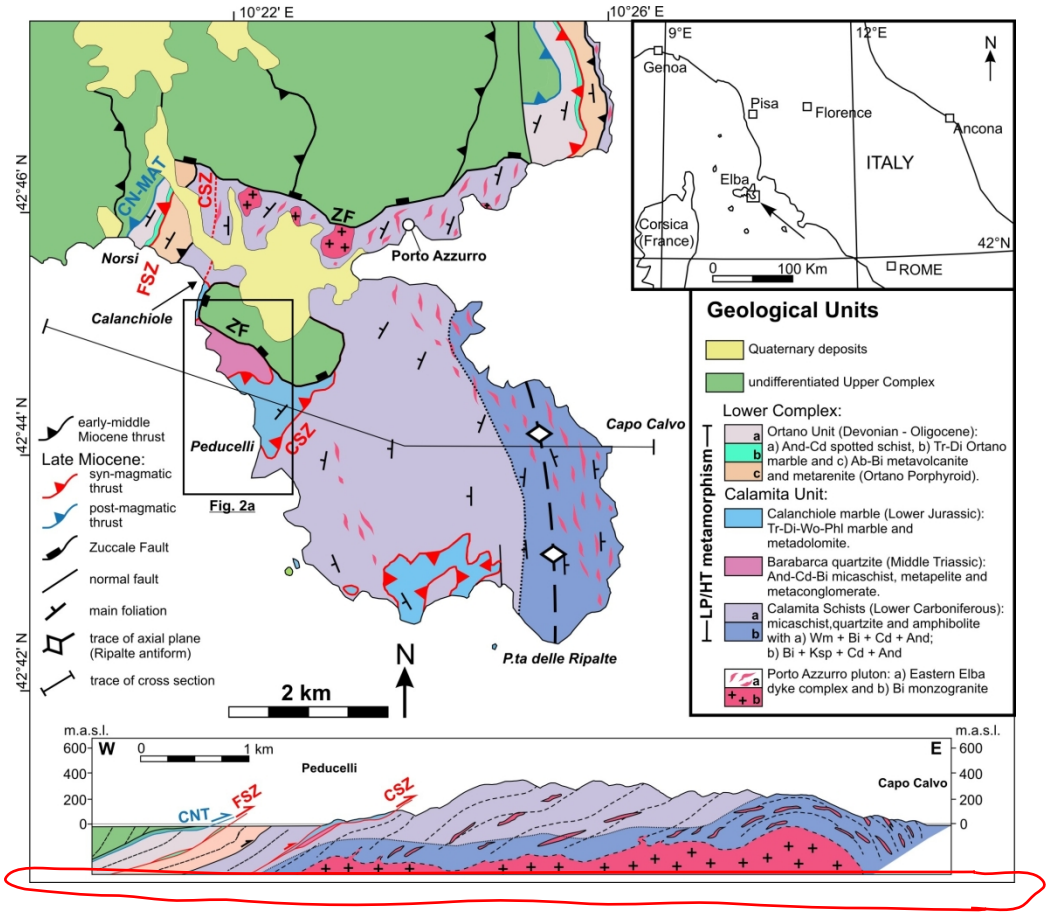

Figure 1 – Simplified structural-geological map of the Calamita peninsula (SE Island of Elba), showing the location of the study area. Abbreviations: CN-MAT: Capo Norsi-Monte Arco Thrust; CSZ: Calanchiole Shear Zone; FSZ: Felciaio Shear Zone. Mineral abbreviations are Ab: albite; And: andalusite; Bi: biotite; Cd: cordierite; Di: diopside; Ksp: K-feldspar; Phl: phlogopite; Tr: tremolite; Wo: wollastonite.

192x169mm (300 x 300 DPI)

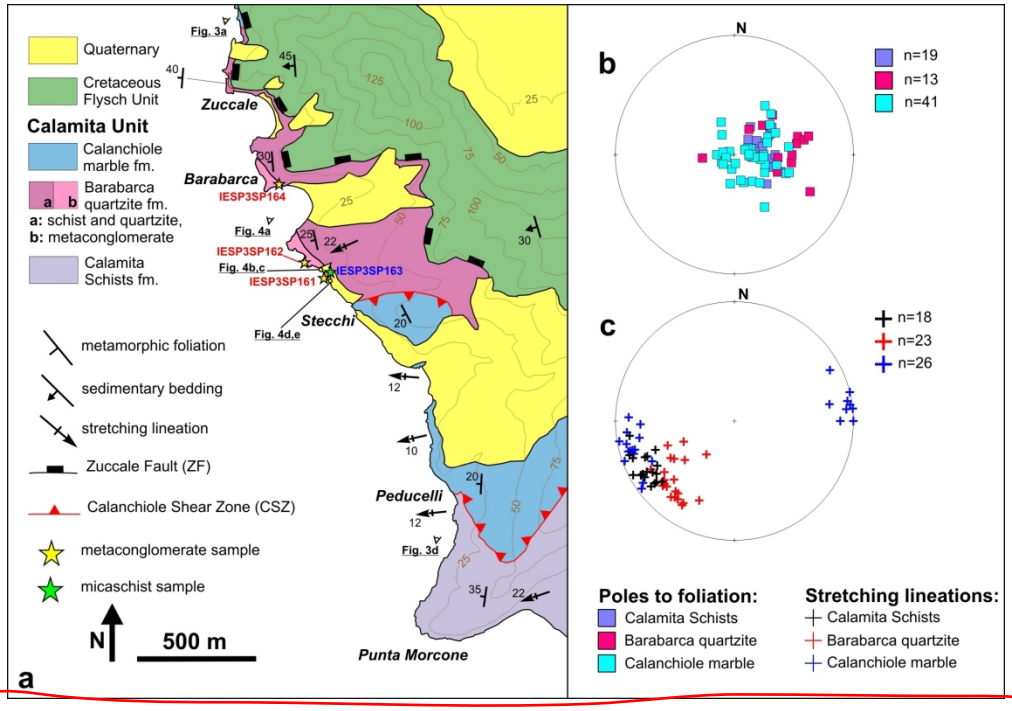

Figure 2 – Detail of the study area. (a) Sketch geological map of the Barabarca area showing the location of figures and samples. (b-c) Stereographic projections (equal area, lower hemisphere) showing (b) poles to foliation and (c) stretching lineations.

185x128mm (300 x 300 DPI)

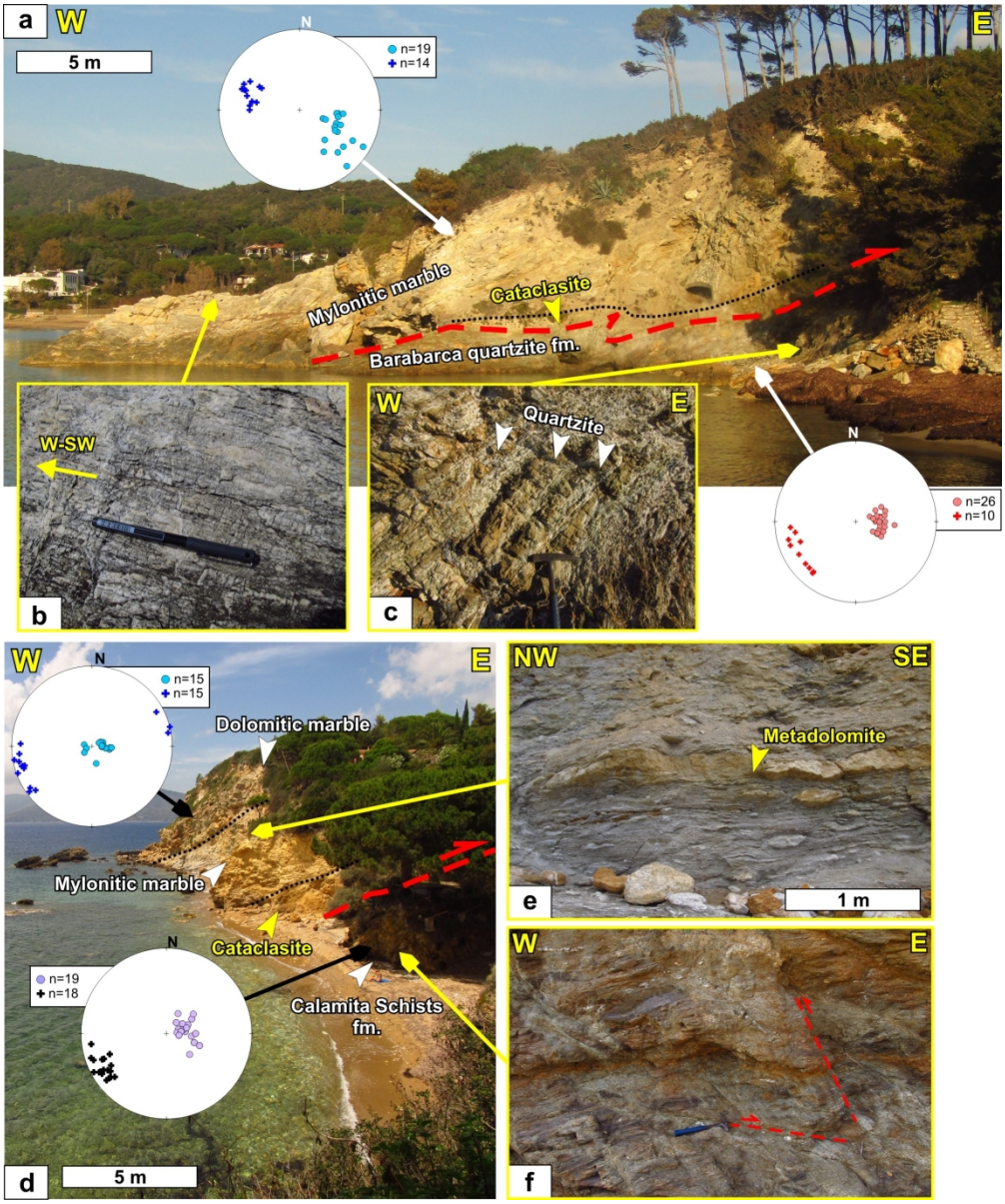

Figure 3 – Relationships between the Calanchiole Shear Zone, the Barabarca quartzite fm., and the Calamita Schists fm., at (a-b-c) Calanchiole and (d-e-f) Peducelli beaches. (a-d) Panoramic views. (b) Stretching lineations, defined by aggregates of dolomite and calcite, in mylonitic marble. (c) Fractured quartzite and schist belonging to the Barabarca quartzite fm. (e) Ultramylonitic marble with boudinated lenses of metadolomite. (f) Riedel shears in the Calamita Schists fm., consistent with overall top-to-the-E sense of shear. Stereographic projections are equal area, lower hemisphere. Circles represent poles to the foliation in the Calanchiole marble fm. (light blue), the Barabarca quartzite fm. (pink), and the Calamita Schists fm. (violet). Crosses are stretching lineations in the Calanchiole marble fm. (blue), the Barabarca quartzite fm. (red), and the Calamita Schists fm. (black) See text for a detailed comment. Measurements from the Calanchiole area after Musumeci & Vaselli (2012).

185x221mm (300 x 300 DPI)

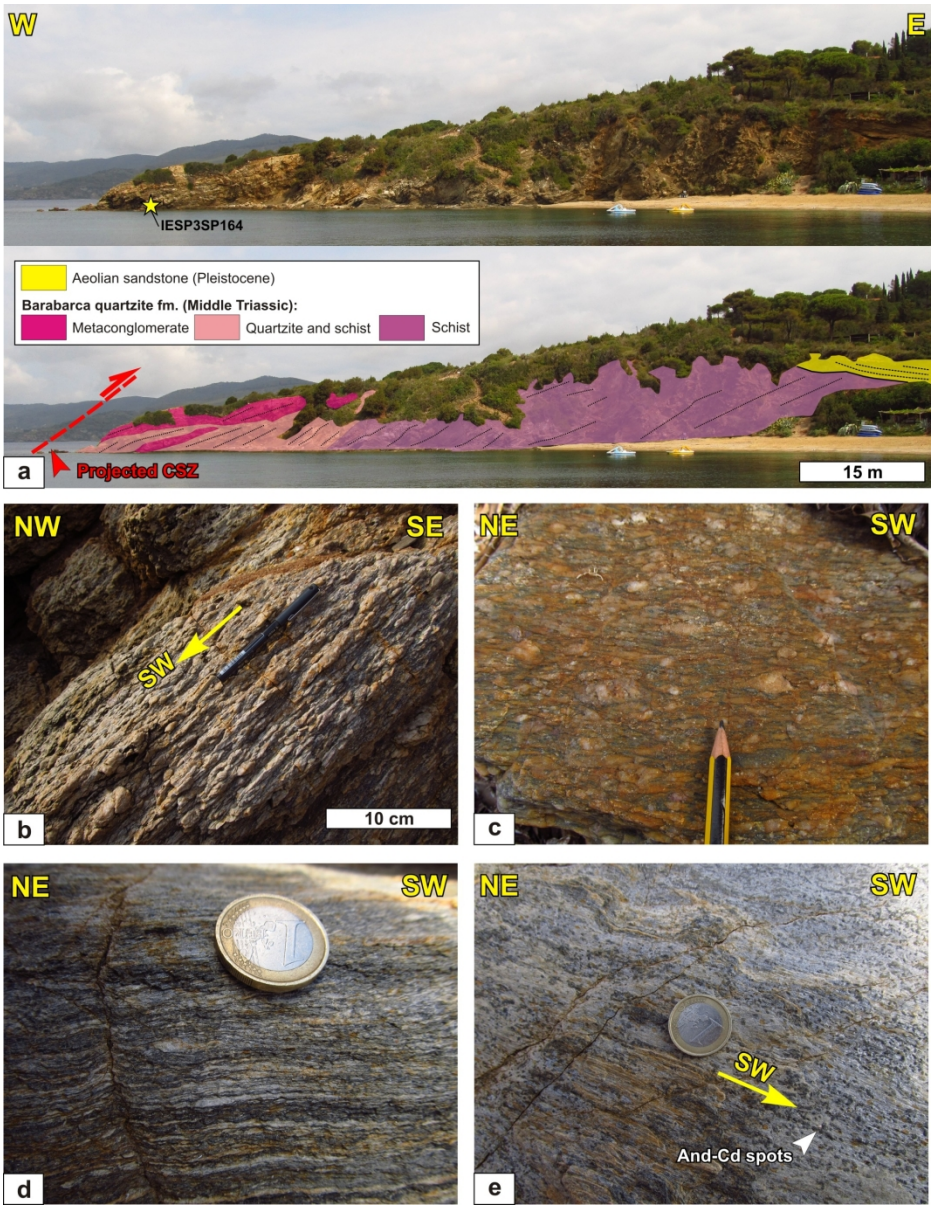

Figure 4 – Details of the investigated outcrops, hosting the metaconglomerate. (a) Panoramic view of the Barabarca gulf, showing the relationships between metaconglomerate, quartzite, and schist in the Barabarca quartzite fm. The red dashed line highlights the projected location of the Calanchiole Shear Zone. (b-c) Outcrop appearance of the deformed quartz metaconglomerate, showing (b) L-tectonite fabric and (c) LS-tectonite fabric. (d-e) Metapelite associated with the metaconglomerate. Note (d) the strong planar fabric, and (e) the presence of stretching lineations defined by quartz fibers and alignments of andalusite (And) - cordierite (Cd) spots.

185x239mm (300 x 300 DPI)

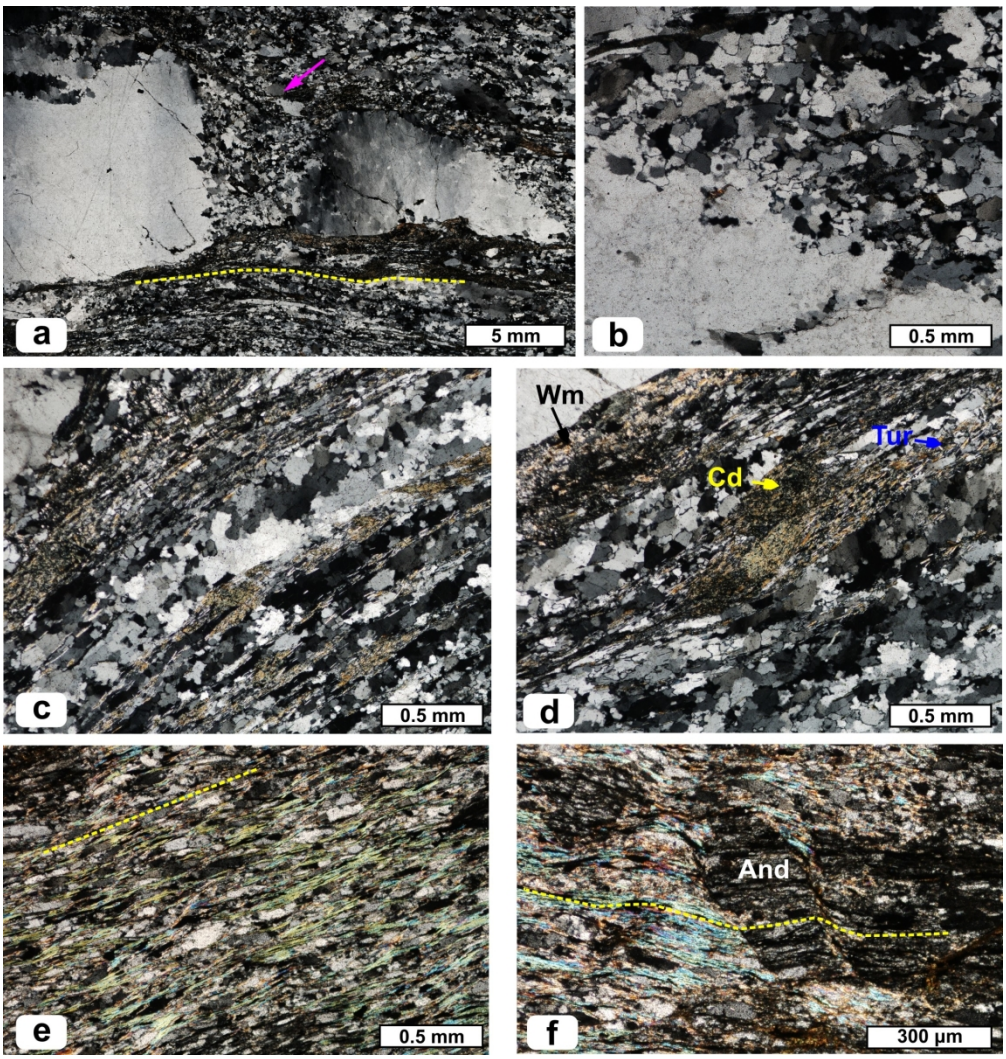

Figure 5 – Representative microstructures of the Barabarca quartzite fm. The yellow dashed line marks the foliation. (a-b-c-d) Quartz metaconglomerate (IESP3SP164): (a) large quartz clasts wrapped by a fine-grained foliated quartz matrix showing boudinage structures (violet arrow); (b) detail of the edge of a deformed quartz clast showing extensive recrystallization; (c) stretched, ribbon-like, quartz clast with amoeboid to lobate boundaries, interlayered with sericite and tourmaline-rich layers; (d) sericitized cordierite and white mica-rich layers associated with tourmaline grains. (e-f) Metapelite (IESP3SP163): (e) detail of the main foliation, defined by the preferred orientation of quartz and phyllosilicates; (f) synkinematic andalusite porphyroblast with rotated internal foliation. And: andalusite; Cd: cordierite. Tur: tourmaline; Wm: white mica.

185x194mm (300 x 300 DPI)

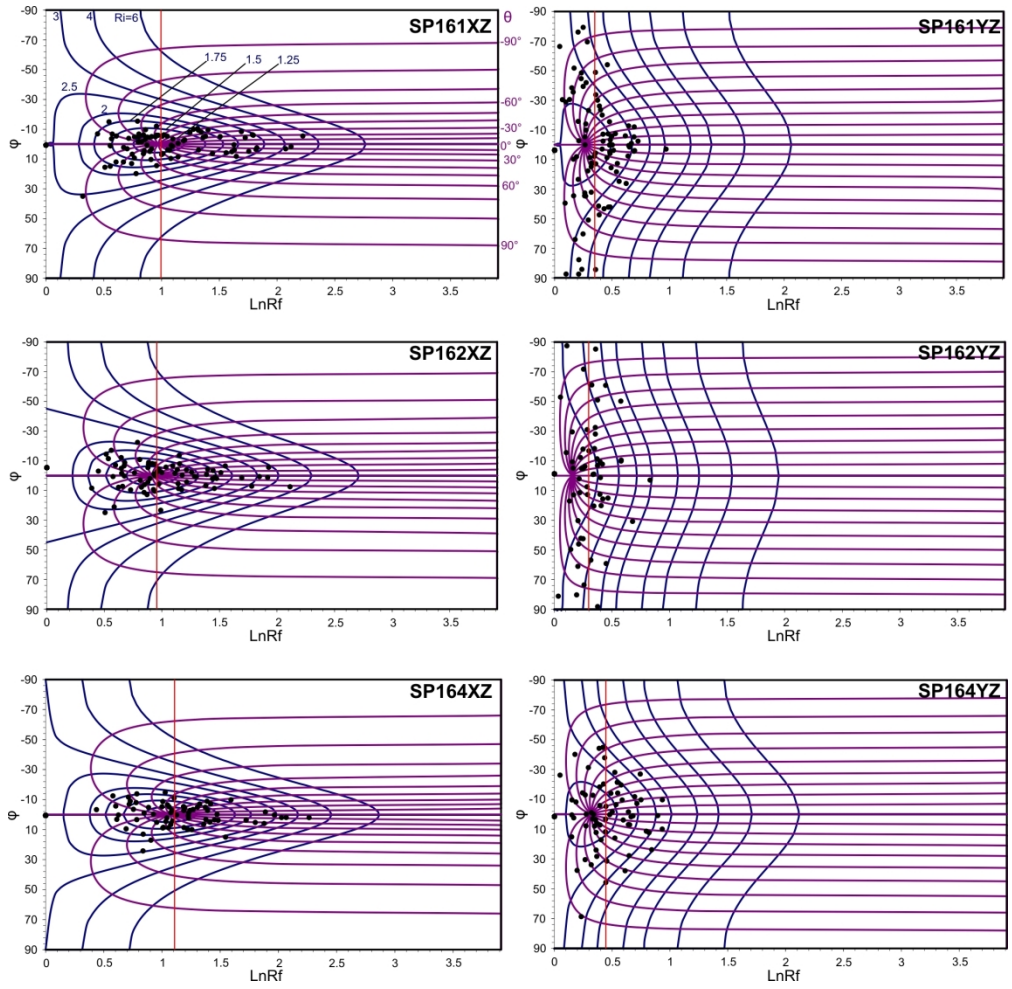

Figure 6 – Detail of the Rf/φ plots used for finite strain analyses on the metaconglomerate samples. Ri contours are shown in blue for Ri = 1.25, 1.5, 1.75, 2, 2.5, 3, 4 and 6. The θ-curves are shown in violet. Red lines represent the vector mean.

183x178mm (300 x 300 DPI)

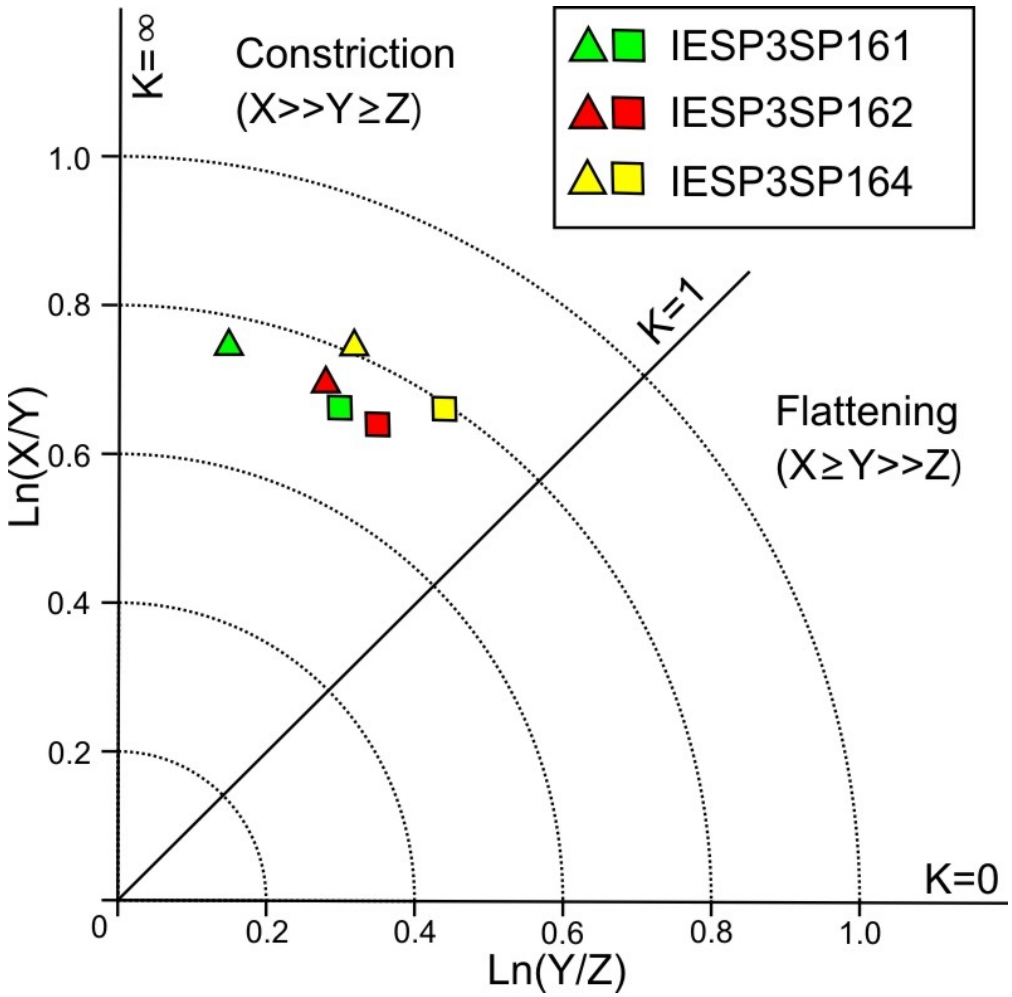

Figure 7 – Results of the finite strain analyses plotted on the Flinn diagram. For each sample, RsXY and RsYZ were calculated based on the harmonic mean method (squares) and the χ2 test (triangles).

67x66mm (300 x 300 DPI)

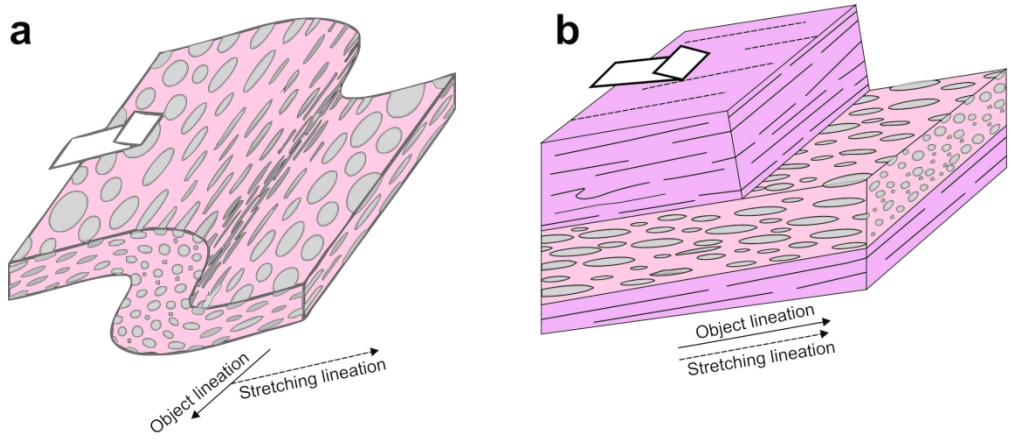

Figure 8 – Block diagrams illustrating the different relationships between object and stretching lineations in the case of (a) constriction by folding in a shear zone and (b) constriction related to strain partitioning in a shear zone. Fig. 8a modified after Sullivan (2013).

200x86mm (300 x 300 DPI)